

# Search for Spectral Irregularities due to Photon–Axionlike-Particle Oscillations with the Fermi Large Area Telescope

M. Ajello,<sup>1</sup> A. Albert,<sup>2</sup> B. Anderson,<sup>3,4</sup> L. Baldini,<sup>5,2</sup> G. Barbiellini,<sup>6,7</sup> D. Bastieri,<sup>8,9</sup> R. Bellazzini,<sup>10</sup> E. Bissaldi,<sup>11</sup> R. D. Blandford,<sup>2</sup> E. D. Bloom,<sup>2</sup> R. Bonino,<sup>12,13</sup> E. Bottacini,<sup>2</sup> J. Bregeon,<sup>14</sup> P. Bruel,<sup>15</sup> R. Buehler,<sup>16</sup> G. A. Caliandro,<sup>2,17</sup> R. A. Cameron,<sup>2</sup> M. Caragiulo,<sup>18,11</sup> P. A. Caraveo,<sup>19</sup> C. Cecchi,<sup>20,21</sup> A. Chekhtman,<sup>22</sup> S. Ciprini,<sup>23,20</sup> J. Cohen-Tanugi,<sup>14</sup> J. Conrad,<sup>3,4,24,\*</sup> F. Costanza,<sup>11</sup> F. D’Ammando,<sup>25,26</sup> A. de Angelis,<sup>27</sup> F. de Palma,<sup>11,28</sup> R. Desiante,<sup>29,12</sup> M. Di Mauro,<sup>2</sup> L. Di Venere,<sup>18,11</sup> A. Domínguez,<sup>1</sup> P. S. Drell,<sup>2</sup> C. Favuzzi,<sup>18,11</sup> W. B. Focke,<sup>2</sup> A. Franckowiak,<sup>2</sup> Y. Fukazawa,<sup>30</sup> S. Funk,<sup>31</sup> P. Fusco,<sup>18,11</sup> F. Gargano,<sup>11</sup> D. Gasparrini,<sup>23,20</sup> N. Giglietto,<sup>18,11</sup> T. Glanzman,<sup>2</sup> G. Godfrey,<sup>2</sup> S. Guiriec,<sup>32,33</sup> D. Horan,<sup>15</sup> G. Jóhannesson,<sup>34</sup> M. Katsuragawa,<sup>35</sup> S. Kensei,<sup>30</sup> M. Kuss,<sup>10</sup> S. Larsson,<sup>36,4</sup> L. Latronico,<sup>12</sup> J. Li,<sup>37</sup> L. Li,<sup>36,4</sup> F. Longo,<sup>6,7</sup> F. Loparco,<sup>18,11</sup> P. Lubrano,<sup>20</sup> G. M. Madejski,<sup>2</sup> S. Maldera,<sup>12</sup> A. Manfreda,<sup>10</sup> M. Mayer,<sup>16</sup> M. N. Mazziotta,<sup>11</sup> M. Meyer,<sup>3,4,†</sup> P. F. Michelson,<sup>2</sup> N. Mirabal,<sup>32,33</sup> T. Mizuno,<sup>38</sup> M. E. Monzani,<sup>2</sup> A. Morselli,<sup>39</sup> I. V. Moskalenko,<sup>2</sup> S. Murgia,<sup>40</sup> M. Negro,<sup>12,13</sup> E. Nuss,<sup>14</sup> C. Okada,<sup>30</sup> E. Orlando,<sup>2</sup> J. F. Ormes,<sup>41</sup> D. Paneque,<sup>42,2</sup> J. S. Perkins,<sup>32</sup> M. Pesce-Rollins,<sup>10,2</sup> F. Piron,<sup>14</sup> G. Pivato,<sup>10</sup> T. A. Porter,<sup>2</sup> S. Rainò,<sup>18,11</sup> R. Rando,<sup>8,9</sup> M. Razzano,<sup>10,43</sup> A. Reimer,<sup>44,2</sup> M. Sánchez-Conde,<sup>4,3,‡</sup> C. Sgrò,<sup>10</sup> D. Simone,<sup>11</sup> E. J. Siskind,<sup>45</sup> F. Spada,<sup>10</sup> G. Spandre,<sup>10</sup> P. Spinelli,<sup>18,11</sup> H. Takahashi,<sup>30</sup> J. B. Thayer,<sup>2</sup> D. F. Torres,<sup>37,46</sup> G. Tosti,<sup>20,21</sup> E. Troja,<sup>32,47</sup> Y. Uchiyama,<sup>48</sup> K. S. Wood,<sup>49</sup> M. Wood,<sup>2</sup> G. Zaharijas,<sup>50,51</sup> and S. Zimmer<sup>3,4</sup>

<sup>1</sup>*Department of Physics and Astronomy, Clemson University,  
Kinard Lab of Physics, Clemson, SC 29634-0978, USA*

<sup>2</sup>*W. W. Hansen Experimental Physics Laboratory,  
Kavli Institute for Particle Astrophysics and Cosmology,  
Department of Physics and SLAC National Accelerator Laboratory, Stanford University, Stanford, CA 94305, USA*

<sup>3</sup>*Department of Physics, Stockholm University, AlbaNova, SE-106 91 Stockholm, Sweden*

<sup>4</sup>*The Oskar Klein Centre for Cosmoparticle Physics, AlbaNova, SE-106 91 Stockholm, Sweden*

<sup>5</sup>*Università di Pisa and Istituto Nazionale di Fisica Nucleare, Sezione di Pisa I-56127 Pisa, Italy*

<sup>6</sup>*Istituto Nazionale di Fisica Nucleare, Sezione di Trieste, I-34127 Trieste, Italy*

<sup>7</sup>*Dipartimento di Fisica, Università di Trieste, I-34127 Trieste, Italy*

<sup>8</sup>*Istituto Nazionale di Fisica Nucleare, Sezione di Padova, I-35131 Padova, Italy*

<sup>9</sup>*Dipartimento di Fisica e Astronomia “G. Galilei”, Università di Padova, I-35131 Padova, Italy*

<sup>10</sup>*Istituto Nazionale di Fisica Nucleare, Sezione di Pisa, I-56127 Pisa, Italy*

<sup>11</sup>*Istituto Nazionale di Fisica Nucleare, Sezione di Bari, I-70126 Bari, Italy*

<sup>12</sup>*Istituto Nazionale di Fisica Nucleare, Sezione di Torino, I-10125 Torino, Italy*

<sup>13</sup>*Dipartimento di Fisica Generale “Amadeo Avogadro”,  
Università degli Studi di Torino, I-10125 Torino, Italy*

<sup>14</sup>*Laboratoire Univers et Particules de Montpellier,  
Université Montpellier, CNRS/IN2P3, Montpellier, France*

<sup>15</sup>*Laboratoire Leprince-Ringuet, École polytechnique, CNRS/IN2P3, Palaiseau, France*

<sup>16</sup>*Deutsches Elektronen Synchrotron DESY, D-15738 Zeuthen, Germany*

<sup>17</sup>*Consorzio Interuniversitario per la Fisica Spaziale (CIFS), I-10133 Torino, Italy*

<sup>18</sup>*Dipartimento di Fisica “M. Merlin” dell’Università e del Politecnico di Bari, I-70126 Bari, Italy*

<sup>19</sup>*INAF-Istituto di Astrofisica Spaziale e Fisica Cosmica, I-20133 Milano, Italy*

<sup>20</sup>*Istituto Nazionale di Fisica Nucleare, Sezione di Perugia, I-06123 Perugia, Italy*

<sup>21</sup>*Dipartimento di Fisica, Università degli Studi di Perugia, I-06123 Perugia, Italy*

<sup>22</sup>*College of Science, George Mason University, Fairfax, VA 22030,  
resident at Naval Research Laboratory, Washington, DC 20375, USA*

<sup>23</sup>*Agenzia Spaziale Italiana (ASI) Science Data Center, I-00133 Roma, Italy*

<sup>24</sup>*Wallenberg Academy Fellow*

<sup>25</sup>*INAF Istituto di Radioastronomia, I-40129 Bologna, Italy*

<sup>26</sup>*Dipartimento di Astronomia, Università di Bologna, I-40127 Bologna, Italy*

<sup>27</sup>*Dipartimento di Fisica, Università di Udine and Istituto Nazionale di Fisica Nucleare,  
Sezione di Trieste, Gruppo Collegato di Udine, I-33100 Udine*

<sup>28</sup>*Università Telematica Pegaso, Piazza Trieste e Trento, 48, I-80132 Napoli, Italy*

<sup>29</sup>*Università di Udine, I-33100 Udine, Italy*

<sup>30</sup>*Department of Physical Sciences, Hiroshima University, Higashi-Hiroshima, Hiroshima 739-8526, Japan*

<sup>31</sup>*Erlangen Centre for Astroparticle Physics, D-91058 Erlangen, Germany*

<sup>32</sup>*NASA Goddard Space Flight Center, Greenbelt, MD 20771, USA*

<sup>33</sup>*NASA Postdoctoral Program Fellow, USA*

<sup>34</sup>*Science Institute, University of Iceland, IS-107 Reykjavik, Iceland*

<sup>35</sup>*Institute of Space and Astronautical Science, Japan Aerospace Exploration Agency,  
3-1-1 Yoshinodai, Chuo-ku, Sagami-hara, Kanagawa 252-5210, Japan*

<sup>36</sup>*Department of Physics, KTH Royal Institute of Technology, AlbaNova, SE-106 91 Stockholm, Sweden*

<sup>37</sup>*Institute of Space Sciences (IEEC-CSIC), Campus UAB, E-08193 Barcelona, Spain*

<sup>38</sup>*Hiroshima Astrophysical Science Center, Hiroshima University, Higashi-Hiroshima, Hiroshima 739-8526, Japan*

<sup>39</sup>*Istituto Nazionale di Fisica Nucleare, Sezione di Roma “Tor Vergata”, I-00133 Roma, Italy*

<sup>40</sup>*Center for Cosmology, Physics and Astronomy Department,  
University of California, Irvine, CA 92697-2575, USA*

<sup>41</sup>*Department of Physics and Astronomy, University of Denver, Denver, CO 80208, USA*

<sup>42</sup>*Max-Planck-Institut für Physik, D-80805 München, Germany*

<sup>43</sup>*Funded by contract FIRB-2012-RBFR12PM1F from the Italian Ministry of Education, University and Research (MIUR)*

<sup>44</sup>*Institut für Astro- und Teilchenphysik and Institut für Theoretische Physik,  
Leopold-Franzens-Universität Innsbruck, A-6020 Innsbruck, Austria*

<sup>45</sup>*NYCB Real-Time Computing Inc., Lattinigtown, NY 11560-1025, USA*

<sup>46</sup>*Institució Catalana de Recerca i Estudis Avançats (ICREA), Barcelona, Spain*

<sup>47</sup>*Department of Physics and Department of Astronomy,  
University of Maryland, College Park, MD 20742, USA*

<sup>48</sup>*Department of Physics, 3-34-1 Nishi-Ikebukuro, Toshima-ku, Tokyo 171-8501, Japan*

<sup>49</sup>*Space Science Division, Naval Research Laboratory, Washington, DC 20375-5352, USA*

<sup>50</sup>*Istituto Nazionale di Fisica Nucleare, Sezione di Trieste,  
and Università di Trieste, I-34127 Trieste, Italy*

<sup>51</sup>*Laboratory for Astroparticle Physics, University of Nova Gorica, Vipavska 13, SI-5000 Nova Gorica, Slovenia*

(Dated: April 25, 2016)

We report on the search for spectral irregularities induced by oscillations between photons and axionlike-particles (ALPs) in the  $\gamma$ -ray spectrum of NGC 1275, the central galaxy of the Perseus cluster. Using six years of *Fermi* Large Area Telescope data, we find no evidence for ALPs and exclude couplings above  $5 \times 10^{-12} \text{ GeV}^{-1}$  for ALP masses  $0.5 \lesssim m_a \lesssim 5 \text{ neV}$  at 95% confidence. The limits are competitive with the sensitivity of planned laboratory experiments, and, together with other bounds, strongly constrain the possibility that ALPs can reduce the  $\gamma$ -ray opacity of the Universe.

## INTRODUCTION

Axions and axionlike-particles (ALPs) are predicted by a variety of extensions of the Standard Model [1–6]. If produced non-thermally in the early Universe, these particles may account for all or a significant fraction of the cold dark matter (DM) [e.g. 7–10], and could be detected through their coupling to photons in magnetic fields [11, 12]. While the axion mass is proportional to its coupling to photons, these two parameters are independent in the case of ALPs.

Photon-ALP interactions could leave an imprint on  $\gamma$ -ray spectra, provided that the ALP mass is sufficiently small,  $m_a \lesssim \mu\text{eV}$ . Above a critical energy  $E_{\text{crit}}$  photon-ALP mixing becomes maximal, leading to a reduction of the photon flux [13–15]. Around  $E_{\text{crit}}$  this is accompanied by spectral irregularities that depend on the strength and morphology of the magnetic field [16]. Photon-ALP conversions could also reduce the opacity of the Universe caused by pair production of  $\gamma$  rays with photons of the extragalactic background light (EBL) [17, 18]. Evidence exists that the  $\gamma$ -ray absorption is indeed lower than expected from state-of-the-art EBL models [19–22], and ALPs have been used to explain these observations [18, 23–26] (see, however, [27, 28]).

Sources embedded in galaxy clusters are promising to search for ALPs due to the strong magnetic fields ex-

tending over large spatial scales in these systems. For example, the absence of irregularities above 200 GeV in the spectrum of the blazar PKS 2155-304, associated with a poor galaxy cluster, has been used to constrain the photon-ALP coupling [29]. Here, we focus on the search for irregularities in the spectrum of the radio galaxy NGC 1275 with the *Fermi* Large Area Telescope (LAT). NGC 1275 is the most favorable target since it is a bright  $\gamma$ -ray emitter detected with a significance exceeding  $100\sigma$  in the third *Fermi*-LAT source catalog (3FGL) [30]. Its broadband emission can be explained with synchrotron-self Compton models, which predict a smooth  $\gamma$ -ray spectrum [31, 32]. It is located at the center of the Perseus cool-core cluster for which rotation measures (RMs) suggest a high central magnetic field [33].

Our analysis makes use of the newest **Pass 8** event-level analysis for LAT data. Compared to previous Passes, **Pass 8** has an improved angular resolution, a broader energy range, larger effective area, as well as reduced uncertainties in the instrumental response functions (IRFs) [34].

## LAT DATA SELECTION

We make use of six years of LAT data taken between Aug. 4, 2008 and Aug. 4, 2014 in the energy range

from 100 MeV to 500 GeV. For lower energies, the effective area decreases rapidly and the energy dispersion increases. At energies above 500 GeV we do not expect sufficient photon statistics [35]. We only consider events that arrive at a zenith angle  $\theta_z < 90^\circ$  in order to minimize the contribution of  $\gamma$  rays from the Earth limb. Time intervals that correspond to bright solar flares and  $\gamma$ -ray bursts are excluded. We extract  $\gamma$ -ray like events within a  $10^\circ \times 10^\circ$  region of interest (ROI) centered at the position of NGC 1275:  $\alpha_{2000} = 3^{\text{h}}19^{\text{m}}49.9^{\text{s}}$ ,  $\delta_{2000} = +41^\circ 30^{\text{m}} 49.2^{\text{s}}$  [30].

Events passing the `Pass 8 P8R2_SOURCE` selection cuts are analyzed using the `P8R2_SOURCE_V6` IRFs.<sup>1</sup> An innovation of the `Pass 8` IRFs is the possibility to subdivide an event class into event types according to the quality of the angular or energy reconstruction (PSF and EDISP event types, respectively). In this analysis we will use the EDISP types to maximize our sensitivity to spectral irregularities. Events are classified into one of four types ranging from EDISP0 to EDISP3, that denote the quality of the energy reconstruction from worst to best. All EDISP event types have a similar number of events in each logarithmic energy bin and are mutually exclusive. The energy dispersion matrices are given in the Supplemental Material [36].

## PHOTON-ALP OSCILLATIONS

Following [e.g. 20, 37–40], we derive the probability  $P_{\gamma\gamma}$  for a final state photon in the photon-ALP beam as a function of energy for an initially un-polarized photon beam (see the Supplemental Material). We expect the irregularities to occur around a critical energy [13],

$$E_{\text{crit}} \sim 2.5 \text{ GeV} \frac{|m_{a,\text{neV}}^2 - \omega_{\text{pl,neV}}^2|}{g_{11} B_{\mu\text{G}}}, \quad (1)$$

with ALP mass  $m_{a,\text{neV}}$  and plasma frequency  $\omega_{\text{pl,neV}}$  in units of neV, coupling constant  $g_{11} = g_{a\gamma}/10^{-11} \text{ GeV}^{-1}$ , and magnetic field  $B_{\mu\text{G}} = B/1 \mu\text{G}$ . We include photon-ALP mixing in the intra-cluster and Galactic magnetic fields [18, 41]. The  $B$  field of the Milky Way is modeled with the coherent component of the model described in [42]. We do not include its turbulent component, as the scales on which the turbulence occurs are usually smaller than the photon-ALP oscillation length. The turbulent intra-cluster  $B$  field is described below. Absorption of  $\gamma$  rays by the EBL is taken into account through the model of [43]. We neglect any oscillations in the intergalactic magnetic field (IGMF). With current upper limits on the IGMF strength of  $\lesssim 10^{-9} \text{ G}$  and on the photon-ALP

coupling,  $g_{11} < 6.6$  [44], we find that  $E_{\text{crit}} \lesssim 100 \text{ GeV}$  only for  $m_{a,\text{neV}} \lesssim 0.5$ . For such low masses,  $g_{11}$  is further constrained below 0.6 from the non-observation of  $\gamma$  rays from SN1987A [45]. Given this small coupling and the comparatively short distance to NGC 1275 (redshift  $z = 0.017559$ ), no strong irregularities should be induced by mixing in the IGMF.

## Intra-cluster magnetic field

Faraday RM observations and magneto-hydrodynamic simulations suggest that the magnetic field in galaxy clusters is turbulent and that its strength follows the electron density  $n_e(r)$  of the intra-cluster medium (ICM),  $B(r) = B_0(n_e(r)/n_e(r=0))^\eta$  [46–48]. We model the turbulent component as a divergence-free homogeneous isotropic field with Gaussian turbulence with zero mean and a variance  $\sigma_B$  [40]. The energy density follows a power law  $M(k) \propto k^q$  in wave numbers  $k$ . It is non-zero only between the minimum and maximum turbulence scales  $k_L = 2\pi/\Lambda_{\text{max}}$  and  $k_H = 2\pi/\Lambda_{\text{min}}$ .

For the Perseus cluster, we use  $n_e(r)$  derived from X-ray observations (Eq. (4) in [49]) within the inner  $r_{\text{max}} = 500 \text{ kpc}$ . Beyond this radius, we conservatively assume a zero magnetic field. RMs currently only probe the innermost region (tens of pc) around NGC 1275. The observations lead to an estimated central magnetic field of  $25 \mu\text{G}$  [33]. An independent lower limit of  $B_0 \gtrsim 2\text{--}13 \mu\text{G}$  for  $0.3 \leq \eta \leq 0.7$  has been derived from MAGIC observations of the Perseus cluster [50]. These results motivate our assumptions for  $\sigma_B = 10 \mu\text{G}$  and  $\eta = 0.5$ , which are also in line with observations of other cool-core clusters [e.g. 51, 52].

For the turbulence spectrum, we assume values derived from RMs of the cool-core cluster A 2199 [52], which has a comparable number of member galaxies. The fiducial parameter choices are summarized in Tab. I.

Parameter	Value
$\sigma_B$	$10 \mu\text{G}$
$r_{\text{max}}$	$500 \text{ kpc}$
$\eta$	$0.5$
$q$	$-2.8$
$\Lambda_{\text{min}}$	$0.7 \text{ kpc}$
$\Lambda_{\text{max}}$	$35 \text{ kpc}$

TABLE I. Fiducial model parameters for the intra-cluster magnetic field in Perseus.

## DATA ANALYSIS

We perform a binned Poisson likelihood analysis, similar to the DM signal search from dwarf spheroidal galax-

<sup>1</sup> [http://www.slac.stanford.edu/exp/glast/groups/canda/lat\\_Performance.htm](http://www.slac.stanford.edu/exp/glast/groups/canda/lat_Performance.htm)

ies [53, 54]. Events are binned into  $10^\circ \times 10^\circ$  sky maps with a resolution of  $0.2^\circ$  per pixel. The width of the logarithmically spaced energy bins is chosen to be 30% of the median energy resolution of each EDISP event type (see the Supplemental Material for details). This results in 39, 67, 94, and 145 energy bins for EDISP0-3, respectively. We have tested with simulations that bin sizes below 40% of the median energy resolution do not affect the results.

For each event type, we perform a fit over the entire energy range and ROI for all source parameters (nuisance parameters  $\theta_i$ ) using *glike* included in the *Fermi-LAT Science Tools* version v10r01p01.<sup>2</sup> We include all point sources listed in the 3FGL within  $15^\circ$  from the ROI center. The diffuse backgrounds are modeled with templates for the Galactic and the isotropic extragalactic  $\gamma$ -ray emission.<sup>3</sup> The energy dispersion is taken into account in the fitting of the point sources whereas it is already accounted for in the data-driven derivation of the diffuse sources. Normalizations of the diffuse sources and point sources within  $8^\circ$  from the ROI center are left free to vary. All spectral indices of the point sources within  $4^\circ$  are also free parameters. The time-averaged spectrum of NGC 1275 is modeled with a logarithmic (log) parabola,  $F(E) = N(E/E_0)^{-(\alpha+\beta \ln(E/E_0))}$ , where  $E_0$  is fixed to 530 MeV [30].

Under the assumption that the profiled nuisance parameters do not change when considering each bin separately [53], we extract the likelihood in each reconstructed energy bin  $k'$ ,  $\mathcal{L}(\mu_{ik'}, \theta_i | D_{ik'})$  as a function of expected counts  $\mu_{ik'}$  of NGC 1275, and observed counts  $D_{ik'}$ . For NGC 1275 a power law with fixed spectral index  $\Gamma = 2$  is now assumed in each bin. For each tested value of  $\mu_{ik'}$  we re-optimize the normalization of the spectrum of the radio galaxy IC 310 which has an angular separation of  $\sim 0.6^\circ$  from NGC 1275.

Under the ALP hypothesis, characterized by  $P_{\gamma\gamma} \equiv P_{\gamma\gamma}(E, m_a, g_{a\gamma}, \mathbf{B}_j)$  for one random turbulent  $B$ -field realization  $\mathbf{B}_j$ , the expected number of photons is calculated through

$$\mu_{ik'} = \sum_k \mathcal{D}_{kk'}^i \int_{\Delta E_k} dE P_{\gamma\gamma} F(E) \mathcal{E}^i(E), \quad (2)$$

where the integration runs over the true energy bin  $\Delta E_k$ ,  $\mathcal{E}^i$  is the exposure, and  $\mathcal{D}_{kk'}^i$  is the energy dispersion for event type EDISP $i$ . Under the null hypothesis,  $P_{\gamma\gamma}$  reduces to the EBL attenuation. The parameters of the intrinsic source spectrum  $F(E)$ ,  $N$ ,  $\alpha$ , and  $\beta$ , are further nuisance parameters. For each tested ALP parameter

and magnetic field, we determine these parameters by profiling the joint likelihood of all energy bins  $k'$

$$\mathcal{L}_i(\boldsymbol{\mu}, \boldsymbol{\theta} | \mathbf{D}) \equiv \prod_{k'} \mathcal{L}(\mu_{ik'}, \theta_i | D_{ik'}), \quad (3)$$

for each event type separately, using the pre-computed likelihood curves  $\mathcal{L}(\mu_{ik'}, \theta_i | D_{ik'})$ . In this way, we treat each event type selection as an independent measurement.<sup>4</sup> The bin-by-bin likelihood curves for the EDISP3 event type are shown in Fig. 1 together with the best-fit spectra.

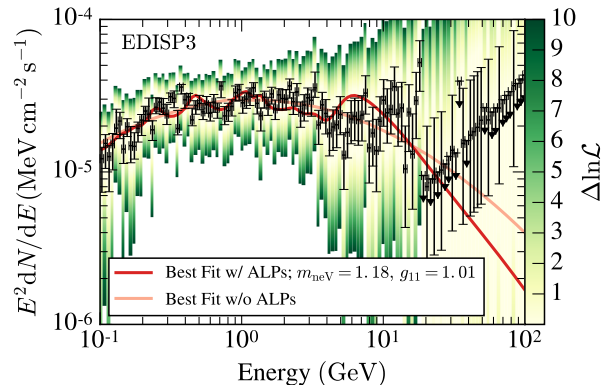


FIG. 1. The likelihood curves (shown in color) for the EDISP3 event type.  $\Delta \ln \mathcal{L} = 0$  corresponds to the maximum likelihood in each bin (black points). The error bars indicate an increase of the likelihood by  $2\Delta \ln \mathcal{L} = 1$ . The best-fit spectrum of the joint likelihood without an ALP (with an ALP with  $m_{\text{neV}} = 1.2$  and  $g_{11} = 1$ ) is shown as a light (dark) red solid line.

We simulate  $N_B = 500$  random realizations of the turbulent field  $\mathbf{B}_j$ ,  $j = 1, \dots, N_B$ . The dependence of the likelihood on the realizations is not easily parametrizable and we cannot assume that the simulations map the space of possible realizations. Therefore, instead of profiling, we sort the  $B$ -field realizations for each tested  $(m_a, g_{a\gamma})$  pair by increasing values of the product over the likelihoods  $\mathcal{L}_i$  and use the realization that corresponds to the  $Q_B = 0.95$  quantile of the likelihood distribution (profiling would correspond to  $Q_B = 1$ ). We will denote this realization as  $\mathbf{B}_{95}$  and the corresponding expected counts with  $\boldsymbol{\mu}_{95}$ . Note that  $\mathbf{B}_{95}$  might be different for different ALP parameters, so that  $\mathbf{B}_{95} \equiv \mathbf{B}_{95}(m_a, g_{a\gamma})$ .

Similar to [55], we evaluate the ALP hypothesis with a likelihood ratio test. The test statistic (TS) for the ALP

<sup>2</sup> <http://fermi.gsfc.nasa.gov/ssc/data/analysis/>

<sup>3</sup> <http://fermi.gsfc.nasa.gov/ssc/data/access/lat/BackgroundModels.html>

<sup>4</sup> This procedure will result in different best-fit estimators for the source parameters for each event type. In this way, it is possible to speed up the optimization considerably. We have verified that our results do not change when the parameters of NGC 1275 are tied over the event types.

hypothesis is calculated from the joint likelihood of all event types:

$$\text{TS} = -2 \sum_i \ln \left( \frac{\mathcal{L}_i(\boldsymbol{\mu}_0, \hat{\boldsymbol{\theta}}|\mathbf{D})}{\mathcal{L}_i(\hat{\boldsymbol{\mu}}_{95}, \hat{\boldsymbol{\theta}}|\mathbf{D})} \right), \quad (4)$$

where  $\boldsymbol{\mu}_0$  are the expected counts for the null (no ALP) hypothesis with maximized nuisance parameters  $\hat{\boldsymbol{\theta}} \equiv \hat{\boldsymbol{\theta}}(\boldsymbol{\mu}_0)$  and  $\hat{\boldsymbol{\mu}}_{95}$  are the expected counts under the ALP hypothesis that, together with  $\hat{\boldsymbol{\theta}}$ , maximize the likelihoods of each event type. We test ALP parameters on a logarithmic  $(m_a, g_{a\gamma})$  grid with  $(19 \times 12)$  steps where  $0.07 \leq m_{a,\text{neV}} \leq 100$  and  $0.1 \leq g_{11} \leq 7$ . The mass range is chosen such that  $E_{\text{crit}}$  falls into the analyzed energy range whereas the maximum coupling is motivated by the bound found in [44]. For the lower bound, the amplitude of the irregularities is too small to be detectable.

In order to convert the TS value into a significance, we need to know the underlying probability distribution. We derive the null distribution from Monte-Carlo simulations and from it the threshold TS value,  $\text{TS}_{\text{thr}}$ , for which we can reject the null hypothesis (see the Supplemental Material for details). For a rejection of the no-ALP hypothesis at a  $3\sigma$  (global) significance level, we find that  $\text{TS} > \text{TS}_{\text{thr}} = 33.1$ .

## RESULTS

The best-fit ALP parameters are found at  $m_{\text{neV}} = 44.6$  and  $g_{11} = 4.76$  with  $\text{TS} = 10.40 < \text{TS}_{\text{thr}}$ , and hence the best fit with ALPs is not significantly preferred over the null hypothesis. We set upper limits by stepping over the ALP parameters and calculating the difference  $\lambda(m_a, g_{a\gamma})$  between the log-likelihood values for each pair  $m_a, g_{a\gamma}$  and the best fit. ALP parameters are excluded with 95% confidence if  $\lambda > \lambda_{\text{thr}} = 22.8$ . The threshold value  $\lambda_{\text{thr}}$  is calculated under the assumption that the probability distribution of the alternative hypothesis follows the null distribution. We have tested this assumption with simulations and found that this choice results in over coverage for ALP parameters causing the strongest irregularities, thus yielding conservative limits.

The excluded parameter space is shown in the left panel of Fig. 2 (black shaded region). Photon-ALP couplings are ruled out between  $0.5 \lesssim g_{11} \lesssim 3$  for  $0.5 \lesssim m_{a,\text{neV}} \lesssim 5$  and  $g_{11} \gtrsim 1$  for  $5 \lesssim m_{a,\text{neV}} \lesssim 10$ . At high masses, the limits run almost parallel to the lines of constant  $E_{\text{crit}}$  (shown as dotted lines for  $B_{\mu\text{G}} = 10$ ). For lower masses, ALP couplings along the  $E_{\text{crit}} = 1$  GeV line with  $1.3 \lesssim g_{11} \lesssim 4$  are not excluded. Around this “hole”-like feature,  $P_{\gamma\gamma}$  exhibits rapid fluctuations for almost the entire *Fermi*-LAT energy range. Given the Poisson noise in the data, these ALP parameters cannot be excluded. We stress that the fit with ALPs is not preferred over the

null hypothesis. For masses below  $m_{a,\text{neV}} = 0.5$ , irregularities still enter the *Fermi*-LAT energy range allowing to exclude ALP parameters.

The observed limits agree well with the expected exclusion region derived from Monte-Carlo simulations (shaded regions). The “hole” feature is not visible in the expected limits but occurs in certain Monte-Carlo realizations (an example is given in the Supplemental Material). In 5% of the simulations (yellow shaded region), ALP parameters are excluded for which the  $E_{\text{crit}} > 100$  GeV. This is expected since we have derived  $\lambda_{\text{thr}}$  from the null distribution where for 5% of the simulations one finds  $\text{TS} > \lambda_{\text{thr}}$ . The parameters for which we could detect an ALP signal at a  $2\sigma$  level agree well with the observed limits (gray hatched region; see the Supplemental Material for details).

The results are subject to systematic uncertainties related to the analysis and magnetic field parameters. Concerning the analysis, changing the energy dispersion has the strongest effect on the limits. If we conservatively broaden the energy dispersion by 20% the area of the tested ALP parameter grid with  $\lambda > 22.8$  decreases by 25%. All other tested effects related to the analysis change the limits at most by  $\sim 4\%$ . Concerning the choice of  $B$ -field parameters, neither the strength, the power spectrum, nor the dependence on the electron density of the magnetic field are well established for Perseus. Therefore, the full analysis is repeated for a magnetic-field strength of  $\sigma_B = 20 \mu\text{G}$ , for a Kolmogorov-type turbulence spectrum,  $q = -11/3$  (as found in the cool-core cluster Hydra A, [e.g. 51]), and by conservatively assuming that the magnetic field is zero beyond  $r_{\text{max}} = 100$  kpc. Increasing  $\sigma_B$  increases the excluded area by 43%. In comparison, the other tested parameters have a subdominant effect of maximally 16%. The dependence of the limits on the particular choice of the EBL model is negligible due to the relative proximity of NGC 1275 ( $z = 0.017559$ ). The absorption is maximally  $\sim 8\%$  at 500 GeV with significantly smaller relative differences for a number of EBL models [43, 56–60]. We provide a comprehensive summary of all tested systematic uncertainties in the Supplemental Material.

The limits derived in this work are compared to other limits and sensitivities of future experiments in Fig. 2 (right). Our results give the strongest constraints to date for  $0.5 \lesssim m_{a,\text{neV}} \lesssim 20$  and surpass the expected limits for the planned ALPS II experiment [61] in that range. They are only a factor of  $\sim 2$  below the exclusion prospects of the planned IAXO experiment [62]. We note that the systematic uncertainties of the future experiments are likely to be smaller than the ones that apply to the present analysis. In conjunction with other limits taken at face value [29, 45, 55], the parameter space where ALPs could explain hints for a lower  $\gamma$ -ray opacity compared to EBL-model predictions (light blue region, [25]) is now strongly constrained. The limits do not constrain ALPs that could

make up the entire DM content of the Universe. This corresponds to the region in Fig. 2 (right) below the  $\theta_1 \mathcal{N} = 1$  line, where  $\mathcal{N}$  is a model dependent factor and  $\theta_1$  is the misalignment angle [10]. Our analysis only constrains ALPs that make up less than 4% of the DM, or equivalently  $\theta_1 \mathcal{N} > 5$ .

Observations with future  $\gamma$ -ray instruments could improve the reported limits and test ALP DM models. The planned Gamma-400 satellite, with an envisaged energy resolution of 1% above 10 GeV [63], might be able to better resolve the spectra and probe higher ALP masses. Higher masses could also be reached with the future Cherenkov Telescope Array (CTA) [64].

It will be possible to reduce the uncertainties of the intra-cluster  $B$  field with the upcoming Square Kilometer Array (SKA) that will conduct a full-sky polarisation survey [65]. It is expected that SKA will observe hundreds of RMs of background sources for the most massive clusters, thereby enabling a more precise determination of their magnetic fields [66].

The analysis presented here can be easily extended to other sources that reside in clusters (e.g. M87 in the Virgo cluster) or in general to any source where ALP-induced spectral irregularities are expected. ALP parameters not constrained in the present analysis (such as those of the “hole”-like feature) could be probed with the different  $B$ -field configurations in other sources.

## ACKNOWLEDGMENTS

The *Fermi*-LAT Collaboration acknowledges support for LAT development, operation and data analysis from NASA and DOE (United States), CEA/Irfu and IN2P3/CNRS (France), ASI and INFN (Italy), MEXT, KEK, and JAXA (Japan), and the K.A. Wallenberg Foundation, the Swedish Research Council and the National Space Board (Sweden). Science analysis support in the operations phase from INAF (Italy) and CNES (France) is also gratefully acknowledged.

---

\* conrad@fysik.su.se

† manuel.meyer@fysik.su.se

‡ sanchezconde@fysik.su.se

- [1] J. Jaeckel and A. Ringwald, Annual Review of Nuclear and Particle Science **60**, 405 (2010), arXiv:1002.0329 [hep-ph].
- [2] R. D. Peccei and H. R. Quinn, Physical Review Letters **38**, 1440 (1977).
- [3] S. Weinberg, Physical Review Letters **40**, 223 (1978).
- [4] F. Wilczek, Physical Review Letters **40**, 279 (1978).
- [5] E. Witten, Physics Letters B **149**, 351 (1984).
- [6] A. Ringwald, Journal of Physics Conference Series **485**, 012013 (2014).
- [7] J. Preskill, M. B. Wise, and F. Wilczek, Physics Letters B **120**, 127 (1983).
- [8] L. F. Abbott and P. Sikivie, Physics Letters B **120**, 133 (1983).
- [9] D. J. E. Marsh, Phys. Rev. D **83**, 123526 (2011), arXiv:1102.4851 [astro-ph.CO].
- [10] P. Arias, D. Cadamuro, M. Goodsell, J. Jaeckel, J. Redondo, and A. Ringwald, JCAP **6**, 013 (2012), arXiv:1201.5902 [hep-ph].
- [11] P. Sikivie, Physical Review Letters **51**, 1415 (1983).
- [12] G. Raffelt and L. Stodolsky, Phys. Rev. D **37**, 1237 (1988).
- [13] D. Hooper and P. D. Serpico, Physical Review Letters **99**, 231102 (2007), arXiv:0706.3203 [hep-ph].
- [14] K. A. Hochmuth and G. Sigl, Phys. Rev. D **76**, 123011 (2007), arXiv:0708.1144.
- [15] A. de Angelis, O. Mansutti, and M. Roncadelli, Physics Letters B **659**, 847 (2008), arXiv:0707.2695.
- [16] D. Wouters and P. Brun, Phys. Rev. D **86**, 043005 (2012), arXiv:1205.6428 [astro-ph.HE].
- [17] A. de Angelis, M. Roncadelli, and O. Mansutti, Phys. Rev. D **76**, 121301 (2007), arXiv:0707.4312.
- [18] M. Simet, D. Hooper, and P. D. Serpico, Phys. Rev. D **77**, 063001 (2008), arXiv:0712.2825.
- [19] A. De Angelis, O. Mansutti, M. Persic, and M. Roncadelli, MNRAS **394**, L21 (2009), arXiv:0807.4246.
- [20] A. de Angelis, G. Galanti, and M. Roncadelli, Phys. Rev. D **84**, 105030 (2011), arXiv:1106.1132 [astro-ph.HE].
- [21] D. Horns and M. Meyer, JCAP **2**, 033 (2012), arXiv:1201.4711 [astro-ph.CO].
- [22] G. Rubtsov and S. Troitsky, JETP Lett. **100**, 397 (2014), arXiv:1406.0239 [astro-ph.HE].
- [23] M. A. Sánchez-Conde, D. Paneque, E. Bloom, *et al.*, Phys. Rev. D **79**, 123511 (2009), arXiv:0905.3270 [astro-ph.CO].
- [24] A. Domínguez, M. A. Sánchez-Conde, and F. Prada, JCAP **11**, 020 (2011), arXiv:1106.1860 [astro-ph.CO].
- [25] M. Meyer, D. Horns, and M. Raue, Phys. Rev. D **87**, 035027 (2013), arXiv:1302.1208 [astro-ph.HE].
- [26] G. Galanti, M. Roncadelli, A. De Angelis, and G. F. Bignami, ArXiv e-prints (2015), arXiv:1503.04436 [astro-ph.HE].
- [27] J. Biteau and D. A. Williams, ApJ **812**, 60 (2015), arXiv:1502.04166.
- [28] A. Domínguez and M. Ajello, ApJ **813**, L34 (2015), arXiv:1510.07913 [astro-ph.HE].
- [29] A. Abramowski, F. Acero, F. Aharonian, *et al.* (H.E.S.S. Collaboration), Phys. Rev. D **88**, 102003 (2013), arXiv:1311.3148 [astro-ph.HE].
- [30] M. Ackermann *et al.* (*Fermi*-LAT Collaboration), Astrophys. J. **810**, 14 (2015), arXiv:1501.06054 [astro-ph.HE].
- [31] J. Aleksić *et al.* (MAGIC Collaboration), A&A **564**, A5 (2014), arXiv:1310.8500 [astro-ph.HE].
- [32] F. Tavecchio and G. Ghisellini, MNRAS **443**, 1224 (2014), arXiv:1404.6894 [astro-ph.HE].
- [33] G. B. Taylor, N. E. Gugliucci, A. C. Fabian, *et al.*, MNRAS **368**, 1500 (2006), astro-ph/0602622.
- [34] W. Atwood, A. Albert, L. Baldini, *et al.*, ArXiv e-prints (2013), arXiv:1303.3514 [astro-ph.IM].
- [35] M. Ackermann *et al.* (The *Fermi*-LAT Collaboration), ApJS **222**, 5 (2016), arXiv:1508.04449 [astro-ph.HE].
- [36] See Supplemental Material, which includes Refs. [68–77], for details on the energy dispersion matrices, the used

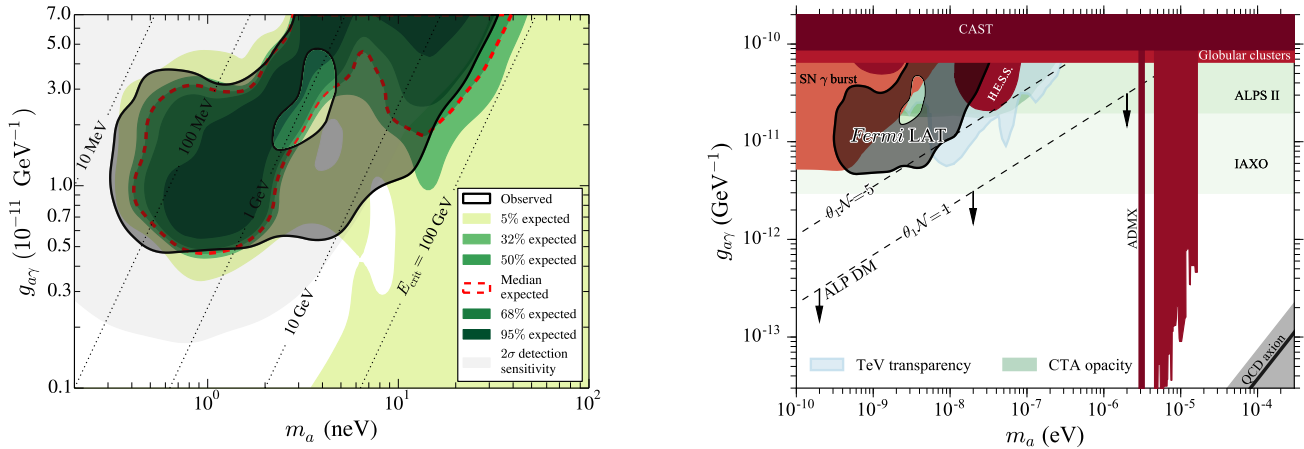


FIG. 2. *Left*: Observed and expected 95% confidence limits on the ALP parameters from 400 Monte-Carlo simulations. Dotted lines correspond to constant critical energies. The hatched gray region shows the parameters where ALPs are detectable at the  $2\sigma$  confidence level (median sensitivity). *Right*: Comparison of *Fermi*-LAT limits with other works. Other Limits are shown in red, expected sensitivities in green. The parameter space where ALPs could explain a low  $\gamma$ -ray opacity is shown in blue. ALPs below the  $\mathcal{N}\theta_1 = 1$  line could account for all the DM. The QCD axion is shown as a gray shaded band and solid black line. See, e.g. [67] and references therein.

- formalism to calculate photon-axionlike-particle oscillations, and details on the statistical method. We also give a comprehensive list of all tested systematic uncertainties.
- [37] Y. Grossman, S. Roy, and J. Zupan, *Physics Letters B* **543**, 23 (2002), hep-ph/0204216.
- [38] C. Csáki, N. Kaloper, M. Peloso, and J. Terning, *JCAP* **5**, 005 (2003), hep-ph/0302030.
- [39] A. Mirizzi, G. G. Raffelt, and P. D. Serpico, in *Axions*, Lecture Notes in Physics, Berlin Springer Verlag, Vol. 741, edited by M. Kuster, G. Raffelt, and B. Beltrán (2008) p. 115, astro-ph/0607415.
- [40] M. Meyer, D. Montanino, and J. Conrad, *JCAP* **9**, 003 (2014), arXiv:1406.5972 [astro-ph.HE].
- [41] D. Horns, L. Maccione, M. Meyer, A. Mirizzi, D. Montanino, and M. Roncadelli, *Phys. Rev. D* **86**, 075024 (2012), arXiv:1207.0776 [astro-ph.HE].
- [42] R. Jansson and G. R. Farrar, *ApJ* **757**, 14 (2012), arXiv:1204.3662 [astro-ph.GA].
- [43] A. Domínguez, J. R. Primack, D. J. Rosario, *et al.*, *MNRAS* **410**, 2556 (2011), arXiv:1007.1459 [astro-ph.CO].
- [44] A. Ayala, I. Domínguez, M. Giannotti, *et al.*, *Phys. Rev. Lett.* **113**, 191302 (2014), arXiv:1406.6053 [astro-ph.SR].
- [45] A. Payez, C. Evoli, T. Fischer, *et al.*, *JCAP* **2**, 006 (2015), arXiv:1410.3747 [astro-ph.HE].
- [46] K. Dolag, A. M. Bykov, and A. Diaferio, *Space Sci. Rev.* **134**, 311 (2008), arXiv:0801.1048.
- [47] Y. Dubois and R. Teyssier, *A&A* **482**, L13 (2008), arXiv:0802.0490.
- [48] L. Feretti, G. Giovannini, F. Govoni, and M. Murgia, *A&A Rev.* **20**, 54 (2012), arXiv:1205.1919 [astro-ph.CO].
- [49] E. Churazov, W. Forman, C. Jones, and H. Böhringer, *ApJ* **590**, 225 (2003), astro-ph/0301482.
- [50] J. Aleksić, E. A. Alvarez, L. A. Antonelli, *et al.* (MAGIC Collaboration), *A&A* **541**, A99 (2012), arXiv:1111.5544 [astro-ph.HE].
- [51] P. Kuchar and T. A. Enßlin, *A&A* **529**, A13 (2011).
- [52] V. Vacca, M. Murgia, F. Govoni, L. Feretti, G. Giovannini, R. A. Perley, and G. B. Taylor, *A&A* **540**, A38 (2012), arXiv:1201.4119 [astro-ph.CO].
- [53] M. Ackermann *et al.* (*Fermi*-LAT Collaboration), *Phys. Rev. D* **89**, 042001 (2014).
- [54] M. Ackermann *et al.* (*Fermi*-LAT Collaboration), *Physical Review Letters* **115**, 231301 (2015), arXiv:1503.02641 [astro-ph.HE].
- [55] D. Wouters and P. Brun, *ApJ* **772**, 44 (2013), arXiv:1304.0989 [astro-ph.HE].
- [56] A. Franceschini, G. Rodighiero, and M. Vaccari, *A&A* **487**, 837 (2008), arXiv:0805.1841.
- [57] J. D. Finke, S. Razzaque, and C. D. Dermer, *ApJ* **712**, 238 (2010), arXiv:0905.1115 [astro-ph.HE].
- [58] T. M. Kneiske and H. Dole, *A&A* **515**, A19+ (2010), arXiv:1001.2132 [astro-ph.CO].
- [59] R. C. Gilmore, R. S. Somerville, J. R. Primack, and A. Domínguez, *MNRAS* **422**, 3189 (2012), arXiv:1104.0671 [astro-ph.CO].
- [60] Y. Inoue, S. Inoue, M. A. R. Kobayashi, R. Makiya, Y. Niino, and T. Totani, *ApJ* **768**, 197 (2013), arXiv:1212.1683.
- [61] R. Bähre, B. Döbrich, J. Dreyling-Eschweiler, *et al.*, *Journal of Instrumentation* **8**, T09001 (2013), arXiv:1302.5647 [physics.ins-det].
- [62] I. G. Irastorza, F. T. Avignone, G. Cantatore, *et al.*, *Journal of Physics Conference Series* **460**, 012002 (2013).
- [63] P. Cumani, A. M. Galper, V. Bonvicini, *et al.*, *ArXiv e-prints* (2015), arXiv:1502.02976 [astro-ph.IM].
- [64] M. Actis, G. Agnetta, F. Aharonian, *et al.* (CTA Consortium), *Experimental Astronomy* **32**, 193 (2011), arXiv:1008.3703 [astro-ph.IM].
- [65] B. M. Gaensler, R. Beck, and L. Feretti, *New Astronomy Reviews* **48**, 1003 (2004), astro-ph/0409100.
- [66] A. Bonafede, F. Vazza, M. Brüggén, T. Akahori,

- E. Carretti, *et al.*, PoS **AASKA14**, 095 (2015), arXiv:1501.00321 [astro-ph.CO].
- [67] M. Meyer and J. Conrad, JCAP **12**, 016 (2014), arXiv:1410.1556 [astro-ph.HE].
- [68] M. Ackermann *et al.* (Fermi-LAT Collaboration), Astrophys.J.Suppl. **203**, 4 (2012), arXiv:1206.1896 [astro-ph.IM].
- [69] A. Mirizzi and D. Montanino, JCAP **12**, 4 (2009), arXiv:0911.0015 [astro-ph.HE].
- [70] A. Mirizzi, G. G. Raffelt, and P. D. Serpico, Phys. Rev. D **76**, 023001 (2007), arXiv:0704.3044.
- [71] A. Dobrynina, A. Kartavtsev, and G. Raffelt, Phys. Rev. D **91**, 083003 (2015), arXiv:1412.4777 [astro-ph.HE].
- [72] N. Bassan, A. Mirizzi, and M. Roncadelli, JCAP **5**, 010 (2010), arXiv:1001.5267 [astro-ph.HE].
- [73] S. S. Wilks, Annals of Mathematical Statistics **9**, 60 (1938).
- [74] G. Cowan, K. Cranmer, E. Gross, and O. Vitells, European Physical Journal C **71**, 1554 (2011), arXiv:1007.1727 [physics.data-an].
- [75] M. Ackermann *et al.* (Fermi-LAT Collaboration), Phys. Rev. **D91**, 122002 (2015), arXiv:1506.00013 [astro-ph.HE].
- [76] A. Albert, G. A. Gómez-Vargas, M. Grefe, C. Muñoz, C. Weniger, E. D. Bloom, E. Charles, M. N. Mazziotta, and A. Morselli, JCAP **10**, 023 (2014), arXiv:1406.3430 [astro-ph.HE].
- [77] A. Bonafede, L. Feretti, M. Murgia, F. Govoni, G. Giovannini, D. Dallacasa, K. Dolag, and G. B. Taylor, A&A **513**, A30 (2010), arXiv:1002.0594 [astro-ph.CO].



# Supplemental Material: Search for Spectral Irregularities due to Photon–Axionlike-Particle Oscillations with the Fermi Large Area Telescope

## Energy dispersion and spectral binning

Event reconstructions prior to **Pass 8** allowed to perform an independent analysis of  $\gamma$ -ray events that convert in either the *front* or *back* part of the LAT tracker, e.g. [68]. With **Pass 8** this is now supplemented with additional *event types* that make it possible to select events based on the quality of the angular reconstruction (PSF event types), or the quality of the energy reconstruction (EDISP event types). Event types within the PSF or EDISP partition are mutually exclusive and each energy bin contains about the same number of events of each type. The analysis presented here is performed for each EDISP type independently. The EDISP event types are defined through the cuts on energy dependent boosted decision tree variables used for the event classification that determine the quality of the event reconstruction.

The exposure-averaged energy dispersion matrix for each event type EDISP $i$  ( $i = 0, 1, 2, 3$ )  $\mathcal{D}_{kk'}^i$  transforms the number of counts in true energy ( $E$ )  $n_k$  in the  $k$ -th energy bin to the number of counts in the  $k'$ -th bin of reconstructed energy ( $E'$ ),  $n_{k'}$ , via

$$n_{k'}^i = \sum_k \mathcal{D}_{kk'}^i n_k^i. \quad (1)$$

We extract  $\mathcal{D}_{kk'}^i$  for six years of observation of NGC 1275 between 30 MeV and 1 TeV in 160 logarithmic-spaced energy bins and evaluate it at the ROI center, i.e. the position of NGC 1275. The resulting matrices are shown in Fig. 3 (left). Clearly, the energy resolution improves from event type EDISP0 to EDISP3.

From the  $\mathcal{D}_{kk'}^i$  we also compute the 68% containment half-width energy resolution  $\Delta E/E$  in the same way as described in [68] (Fig. 3, right). At 10.2 GeV the energy resolution improves from 16% for EDISP0 to 4% for EDISP3 (using the half width of  $\Delta E/E$ ). From the full-width energy resolution, we choose the number of logarithmic spaced energy bins used in the analysis. The number of bins should be small enough to resolve the photon-ALP spectral features after convolving them with the energy dispersion. As a compromise between computational time and energy resolution, we choose a bin size of 30% of the median energy resolution  $\langle \Delta E/E \rangle$ . The total number of bins for each event type EDISP $i$  is then

$$N_{\text{bin}} = \left\lceil \frac{\log_{10}(E_{\text{max}}/E_{\text{min}})}{0.3 \langle \Delta E/E \rangle^i} \right\rceil, \quad (2)$$

with  $E_{\text{min}} = 100$  MeV and  $E_{\text{max}} = 500$  GeV. Since we forward fold the model spectrum with the detector response (Eq. (2) in the main article), bin-by-bin correlations are self-consistently accounted for.

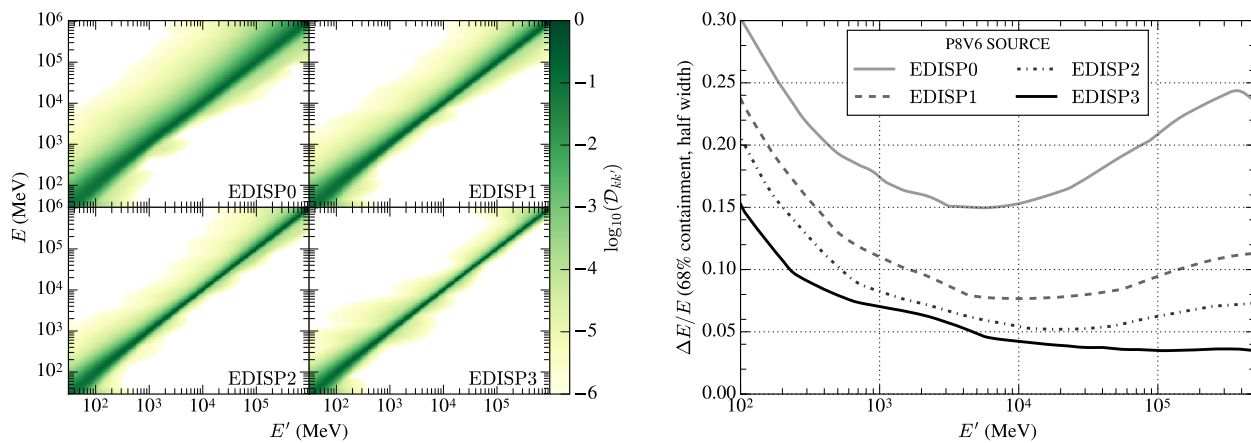


FIG. 3. *Left*: Exposure-weighted energy dispersion matrices for the four EDISP types in **Pass 8**. *Right*: Energy resolution (half-width of the 68% containment) of all event types derived from the energy dispersion matrices.

### Modelling Photon-ALP oscillations

We describe the photon-ALP beam of energy  $E$  in terms of the density matrix  $\rho = \Psi \otimes \Psi^\dagger$ , where  $\Psi = (A_1, A_2, a)^T$  is a photon-ALP state with photon polarizations  $A_{1,2}$  and the ALP field strength  $a$ . Assuming the beam to propagate along the  $x_3$  direction and neglecting photon absorption, the evolution of the system along  $x_3$  is described with the Von-Neumann-like commutator equation, e.g. [69],

$$i \frac{d\rho}{dx_3} = [\rho, \mathcal{M}], \quad (3)$$

with the mixing matrix  $\mathcal{M}$ . The photon-ALP mixing is induced by the transversal magnetic field  $\mathbf{B}_\perp$  only. For a homogenous field orientated along  $x_2$ ,  $\mathbf{B}_\perp = B\hat{\mathbf{e}}_2$ , the mixing matrix reads [12, 70],

$$\mathcal{M} = \begin{pmatrix} \Delta_\perp & 0 & 0 \\ 0 & \Delta_\parallel & \Delta_{a\gamma} \\ 0 & \Delta_{a\gamma} & \Delta_a \end{pmatrix}, \quad (4)$$

where Faraday rotation is neglected. The  $\Delta$  terms give the momentum differences between the polarization states. The terms  $\Delta_\perp = \Delta_{\text{pl}} + 2\Delta_{\text{QED}}$  and  $\Delta_\parallel = \Delta_{\text{pl}} + (7/2)\Delta_{\text{QED}}$  describe the propagation of photons in a plasma with plasma frequency  $\omega_{\text{pl}}$ , where  $\Delta_{\text{pl}} = -\omega_{\text{pl}}^2/2E$ . They also include the QED vacuum polarization through  $\Delta_{\text{QED}} = \alpha EB^2/45\pi B_{\text{cr}}^2$ , with the critical magnetic field  $B_{\text{cr}} \sim 4.4 \times 10^{13}$  G and the fine-structure constant  $\alpha$ . For the energies and magnetic fields under consideration, this term is, however, completely negligible. The same holds for an additional photon dispersion term [71] since we neglect photon-ALP mixing in the intergalactic medium beyond the galaxy cluster. Photon-ALP mixing is induced by the off-diagonal term  $\Delta_{a\gamma} = g_{a\gamma}B/2$ . The kinetic term for the ALP is  $\Delta_a = -m_a^2/2E$ . Numerical values for the momentum differences in suitable units are given in e.g. [41]. The oscillation length is given by  $L = 2\pi/\Delta_{\text{osc}}$ , where  $\Delta_{\text{osc}} = [(\Delta_a - \Delta_\parallel)^2 - 4\Delta_{a\gamma}^2]^{1/2}$ . For a 10 GeV  $\gamma$  ray and  $B_{\mu\text{G}} = 10$ ,  $m_{a,\text{meV}} = 10$ , and  $g_{11} = 1$ , one finds  $L \sim 7.5$  kpc. For the considered profile of the electron density (Eq. (4) in [49]), the plasma frequency is at most 10% of the minimum ALP mass considered. Therefore,  $\Delta_a - \Delta_\parallel \sim \Delta_a$ , making the critical energy (Eq. (1) in the main article) essentially independent of  $\omega_{\text{pl}}$ .

Equation (3) is solved by means of the transfer matrix  $\mathcal{T}$ ,  $\rho(x_3) = \mathcal{T}(x_3, 0; E)\rho(0)\mathcal{T}^\dagger(x_3, 0; E)$ , with the initial condition  $\mathcal{T}(0, 0; E) = 1$ , e.g. [17, 23, 38, 72]. Neither the magnetic field in the Perseus cluster nor the Galactic magnetic field are homogeneous. Therefore, the path in the different  $B$  fields is split up into  $N$  segments. In each segment,  $\mathbf{B}_\perp$  is assumed to be constant and forms an angle  $\psi_i$ , ( $i = 1, \dots, N$ ) with the  $x_2$  axis. The  $B$  field is modeled as a divergence-free homogeneous isotropic field with Gaussian turbulence [40] The full transfer matrix is then

$$\mathcal{T}(x_{3,N}, x_{3,1}; \psi_N, \dots, \psi_1; E) = \prod_{i=1}^N \mathcal{T}(x_{3,i+1}, x_{3,i}; \psi_i; E). \quad (5)$$

In this setup, the probability to observe a photon of either polarization  $\rho_{jj} = \text{diag}(\delta_{1j}, \delta_{2j}, 0)$  after the  $N$ -th domain is given by

$$P_{\gamma\gamma} = \sum_{j=1,2} \text{Tr}(\rho_{jj}\mathcal{T}\rho_0\mathcal{T}^\dagger). \quad (6)$$

For the initial polarization, we assume an un-polarized pure  $\gamma$ -ray beam,  $\rho_0 = (1/2)\text{diag}(1, 1, 0)$ . For the fiducial parameters of the Perseus cluster, the Galactic magnetic field of Ref. [42], and the EBL model of Ref. [43], the photon survival probability for one ALP mass and coupling is shown in Fig. 4 for 500 random realizations of the cluster magnetic field.

### Null distribution and confidence intervals

The usual procedure to convert a TS value into a significance with which one can reject the null hypothesis using Wilks' Theorem [73] cannot be applied in the present analysis. First of all, the spectral irregularities do not scale linearly with the ALP parameters. Secondly, under the null hypothesis, the likelihood values are independent of the magnetic-field realizations which are additional nuisance parameters under the alternative hypothesis. Thirdly, photon-ALP oscillations are completely degenerate in coupling and magnetic field since the oscillation strength scales

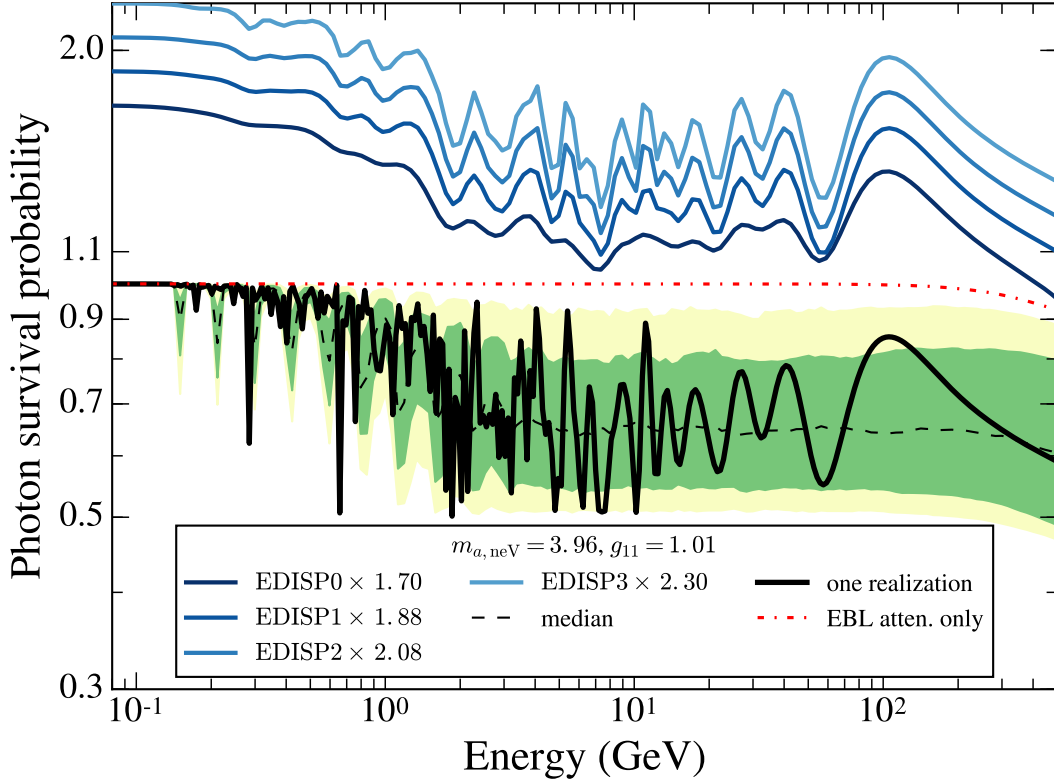


FIG. 4. Example of the photon survival probability for an ALP with mass  $m_{a,\text{neV}} = 3.96$  and coupling  $g_{11} = 1.01$ . The green (yellow) shaded region shows the 68% (95%) containment of 500 realizations of the turbulent cluster  $B$  field. The blue lines show  $P_{\gamma\gamma}$  for one realization (black solid line) convolved with the energy dispersion of the different event types (from bottom to top EDISP0-3). They are scaled upwards for better visibility. The EBL attenuation sets in above 100 GeV (red dash-dotted line).

with  $\Delta_{a\gamma}$ , leading to potential correlations between the different tested ALP parameters. For these reasons, the null distribution is a priori unknown and needs to be derived from Monte-Carlo simulations.

We simulate  $N_{\text{PE}} = 400$  six year data sets (pseudo experiments, PEs) within a  $20^\circ \times 20^\circ$  ROI including all 3FGL point sources and the isotropic backgrounds for each event type between 30 MeV and 1 TeV. We perform these simulations with an energy window and ROI larger than the ones used in the analysis in order to account for a possible migration of photons between adjacent energy bins or sky regions due to the PSF and energy dispersion. All point sources, including NGC 1275, are simulated with energy dispersion, whereas we disable it for the diffuse templates. The actual pointing history of the LAT is used in the simulations. No ALP signal is included. We perform the exact same analysis as done on the data on each PE and calculate the TS values as the difference between the maximum likelihood and the profile likelihood of the fit without ALPs. For one PE, we show the resulting exclusion region in comparison with the data in Fig. 5 (left). The figure illustrates that the complex behavior of the exclusion region is already evident in Monte-Carlo simulations. The full null distribution is shown in Fig. 5 (right). It can be parametrized with a non-central  $\chi^2$  distribution with 10.09 degrees of freedom (d.o.f.) and non-centrality parameter  $s = 2.51$ . For these parameters the Kolmogorov-Smirnov test yields a  $p$ -value of 0.70. All TS values are larger than zero indicating that all fits including ALPs are preferred. This is expected since we have deliberately chosen a high quantile  $Q_B = 0.95$ . Selecting a smaller quantile would shift the distribution towards zero as  $B$ -field realizations would be selected that lead to a worse fit to the data. In order to avoid false ALP detections we use the null distribution to derive the threshold TS value,  $\text{TS}_{\text{thr}}$ , for which evidence for ALPs could be claimed at a  $3\sigma$  ( $2\sigma$ ) confidence level. From the fit to the null distribution one finds that  $\text{TS}_{\text{thr}} = 33.1^{+5.3}_{-5.8}$  ( $23.1^{+1.8}_{-1.2}$ ). The uncertainties are at 68% confidence and are derived from bootstrapping the null distribution  $10^4$  times.

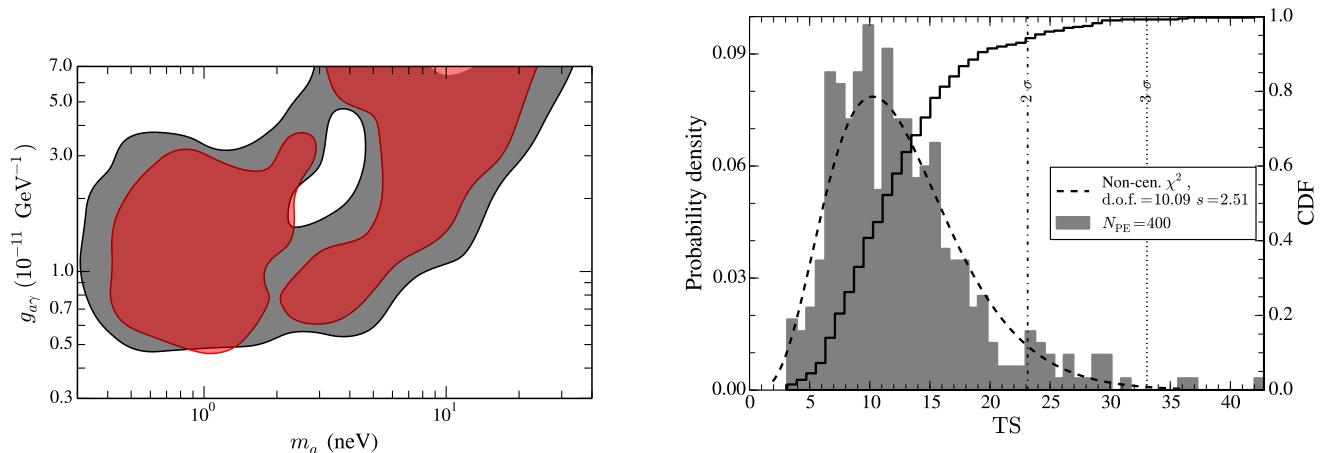


FIG. 5. *Left*: Excluded parameter space from the data (black shaded region), and for one PE (red shaded region). *Right*: Null distribution of TS values for  $N_{\text{PE}} = 400$  and  $Q_B = 0.95$ . The dashed line represents a fit to the data with a non-central  $\chi^2$  distribution. The cumulative distribution function (CDF) is shown as a black solid line. The dash-dotted (dotted) vertical line shows the threshold TS value that corresponds to a  $2\sigma$  ( $3\sigma$ ) confidence level.

Since we are deriving  $\text{TS}_{\text{thr}}$  from simulations, one could ask why we are choosing  $Q_B = 0.95$  instead of profiling, i.e.,  $Q_B = 1$ . The reason is that we can only test a limited number of  $B$ -field realizations, thereby probably missing the one actually realized in nature. While the profile likelihood ( $Q_B = 1$ ) is sensitive to the number of tested  $B$ -field realizations, we find that with  $Q_B = 0.95$  our analysis is insensitive to the ad-hoc choice of number of realizations. Furthermore, we find better coverage for this choice, as discussed below.

We derive the ALP parameters that are detectable at a certain significance using an Asimov data set, i.e. setting the observed counts equal to the expected number of counts [74]. For each ALP parameter and  $B$ -field realization we calculate the expected number of counts using Eq. (2) of the main article assuming the spectral parameters of NGC 1275 that are given in the 3FGL. The obtained Asimov data are subsequently fitted with a log parabola without an ALP contribution. As before, for each tested ALP parameter pair, we sort the likelihood values for the different  $B$ -field realizations and evaluate the test statistic for the realization that corresponds to the  $Q_B = 0.95$  quantile,

$$\text{TS}_A = -2 \sum_i \ln \left( \frac{\mathcal{L}_i(\boldsymbol{\mu}_0, \hat{\boldsymbol{\theta}} | \boldsymbol{\mu}_{95})}{\mathcal{L}_i(\hat{\boldsymbol{\mu}}_{95}, \hat{\boldsymbol{\theta}} | \boldsymbol{\mu}_{95})} \right), \quad (7)$$

where the subscript A denotes the Asimov data set. An ALP signal could be detectable at a  $2\sigma$  level where  $\text{TS}_A > 23.1$ , shown as the gray hatched region in Fig. 2 (left) of the main article.

For the same reasons that make it necessary to derive the null distribution from Monte-Carlo simulations, we cannot assume that it is possible to derive upper limits on the ALP mass and coupling by increasing the log likelihood by  $\lambda_{\text{thr}} = 5.99$ .<sup>5</sup> The  $\lambda$  values are given by the log-likelihood ratio test between the likelihood with a certain ALP mass and coupling with conditionally maximized nuisance parameters  $\hat{\boldsymbol{\theta}}(m_a, g_{a\gamma}, \mathbf{B}_{95})$  and the unconditionally maximized likelihood,

$$\lambda(m_a, g_{a\gamma}) = -2 \sum_{i,k'} \ln \left( \frac{\mathcal{L}(m_a, g_{a\gamma}, \mathbf{B}_{95}, \hat{\boldsymbol{\theta}}(m_a, g_{a\gamma}, \mathbf{B}_{95}) | D_{ik'})}{\mathcal{L}(\hat{m}_a, \hat{g}_{a\gamma}, \mathbf{B}_{95}, \hat{\boldsymbol{\theta}} | D_{ik'})} \right). \quad (8)$$

In the above equation,  $\hat{m}_a$ ,  $\hat{g}_{a\gamma}$ , and  $\hat{\boldsymbol{\theta}}$  denote the maximum likelihood estimators. As before, we have chosen the magnetic field  $\mathbf{B}_{95}$  that corresponds to the  $Q_B = 0.95$  quantile of the distribution of likelihoods with respect to the  $B$ -field realizations. Ensuring coverage would in principle require to simulate the distribution of  $\lambda(m_a, g_{a\gamma})$  (*alternative distribution*) for the complete parameter space, which is not feasible. We therefore make the ansatz that

<sup>5</sup> This value corresponds to a  $2\sigma$  confidence limit in case of a  $\chi^2$

distribution with 2 d.o.f. (ALP mass and coupling).

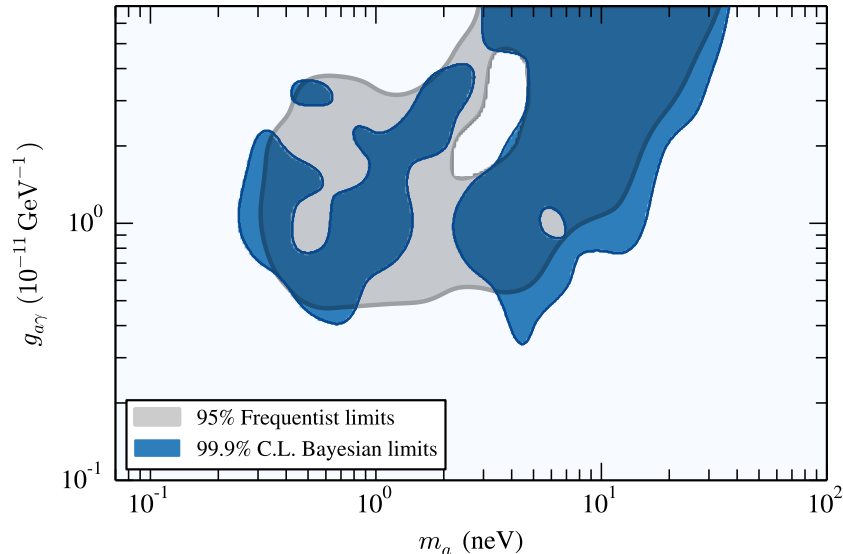


FIG. 6. Comparison between 99.9% Bayesian and frequentist upper limits. See text for further details.

the alternative distribution for each tested ALP parameter is equal to the null distribution. From the non-central  $\chi^2$  fit to the null distribution we find that  $\lambda_{\text{thr}} = 22.8$  corresponds to a 95% upper limit (cf. Fig. 5, right). For this choice, the expected limits (median sensitivity) agree well with the ALP parameters for which a signal could be detected (see Fig. 2, left, of the main article). We examine the coverage with simulations where we multiply the intrinsic spectrum of NGC 1275 with the photon survival probability including ALPs. We test seven ALP parameter pairs with masses between 1 and 60 neV and couplings between 0.5 and  $7 \times 10^{-11} \text{ GeV}^{-1}$ , and simulate 100 PEs for each parameter pair. By construction, we find correct coverage for ALP parameters that result in weak irregularities or irregularities largely outside the *Fermi*-LAT energy range. In these cases we expect the alternative distribution to be close to the null distribution. For masses and couplings where the ALP effect is strongest, we consistently find over coverage, thus making our results conservative. The over coverage becomes more severe if we select  $Q_B = 0.5$  or if we treat the magnetic field in a Bayesian fashion by taking the average over the  $B$ -field realizations. For  $Q_B = 1$ , the trend reverses and we find under coverage.

We have also carried out a Bayesian analysis with flat priors on the magnetic-field realizations and logarithmic flat priors for  $m_a$  and  $g_{a\gamma}$ . We find the limits corresponding to a  $(1 - \alpha)$  confidence level by integrating over the posterior probability where we sort by decreasing likelihood values. Studying the coverage of the limits, we find under coverage for the same injected ALP signals as above. Therefore, we compare the 99.9% C.L. Bayesian limits (resulting in coverage  $> 95\%$ ) with the frequentist limits which give coverage  $> 95\%$  in Fig. 6. The Bayesian limits exclude 3% less of the parameter space than the frequentist analysis. The shape of the excluded region is comparable in the two analyses.

### Systematic Uncertainties

We investigate how the systematic uncertainties connected to the LAT instrument, to the analysis choices, and to the choices for the magnetic-field parameters affect the derived bounds on the ALP parameters. We quantify the importance of each systematic uncertainty by studying the change of the excluded area  $\alpha_{\text{sys}}$ , i.e. the area of the tested ALP parameter space for which  $\lambda > \lambda_{\text{thr}}$ . All examined systematics and the respective values of  $\alpha_{\text{sys}}$  are summarized in Tab. II. In the following, we discuss each source of systematic uncertainty in further detail.

Systematic test	$\alpha_{\text{sys}}$
Bin-by-bin power-law index	-4 %
Bracketing of the effective area	-2 %
Broadening of energy dispersion by 20 %	-25 %
Central magnetic field $\sigma_B = 20 \mu\text{G}$	+43 %
Kolmogorov turbulence spectrum $q = -11/3$	+12 %
Maximum spatial extent of magnetic field $r_{\text{max}} = 100 \text{ kpc}$	-16 %

TABLE II. Summary of systematic effects and their effect on the ALP bounds quantified by the change in the excluded area,  $\alpha_{\text{sys}}$ , of the ALP parameter space induced by the corresponding effect.

### LAT instrument and analysis

*Assumed power-law index for bin-by-bin likelihood.* In the extraction of the likelihood curves as a function of the expected counts in each energy bin we have assumed a power law with spectral index  $\Gamma = 2$  for NGC 1275. Since the bin size is chosen as 30 % of the median energy resolution, the bin-by-bin likelihood should essentially be independent of the assumed spectral shape. We test this by repeating the ALP the analysis for power-law indices of  $\Gamma = 2.5$  and  $\Gamma = 1.5$ . As expected, the excluded area in the tested parameter space only changes marginally. Indeed, it decreases by  $\alpha_{\text{sys}} = 4\%$  for  $\Gamma = 1.5$  whereas it is unchanged for  $\Gamma = 2.5$ .

*Bracketing of the effective area.* The systematic uncertainty for the effective area is assessed using the IRF bracketing method [68]. The exposure is scaled with  $(1 + \epsilon(E)B(E))$ , where  $\epsilon(E)$  is the relative uncertainty of the effective area and we take  $B(E) = \pm 1$ . For an analysis making use of the individual event types it is recommended to assume a relative uncertainty of 10 % between 100 MeV and 100 GeV. It increases linearly with the logarithm of energy to 20 % at 30 MeV and 1 TeV<sup>6</sup>. Using this scaling and repeating the analysis, we find a decrease by  $\alpha_{\text{sys}} = 2\%$  for  $B = +1$ . For  $B = -1$ , the results remain unchanged. The small change of the limits is anticipated since we are interested in spectral irregularities that are not affected by an overall scaling of the effective area.

*Small-scale structures in the effective area.* We assess the possibility that unmodeled structures exist in the effective area. Such structures might mimic spectral irregularities induced by ALPs. We follow a similar approach as in [75] and estimate the strength of such structures from the residuals of a spectral analysis of bright  $\gamma$ -ray sources. At low energies (100 MeV–5 GeV) we consider the Vela pulsar and for higher energies (5 GeV–100 GeV) the Earth limb. The basic data selections are summarized in Tab. III.<sup>7</sup> All other analysis choices are the same as for the main analysis of NGC 1275.

For the Vela pulsar, we calculate the pulsar phases  $\varphi$  using the standard ephemeris<sup>8</sup> and the *tempo2* package<sup>9</sup>. The spectral parameters of the background sources are determined separately for each EDISP event type in the off-pulse interval  $\varphi \in [0.7, 1]$  using the standard binned analysis pipeline of the *Fermi-LAT Science Tools*. The parameters are taken as an input for the phase averaged fit including the Vela pulsar. As in the 3FGL, the Vela spectrum is modeled with a power law with a super-exponential cutoff.<sup>10</sup> We show the fit residuals over the entire ROI in Fig. 7.

The Earth limb  $\gamma$  rays are produced by cosmic-ray interactions in the Earth's upper atmosphere. Therefore, the limb data set predominantly comprises  $\gamma$  rays that arrive at a rocking angle  $> 52^\circ$  and in the zenith angle range  $111.1002^\circ < \theta_z < 112.9545^\circ$  (*On* region). For the astrophysical background, photons within  $108.6629^\circ < \theta_z < 109.5725^\circ$  and  $114.5193^\circ < \theta_z < 115.4675^\circ$  are considered (*Off* regions). The zenith angle cuts are chosen such that the solid angle for the *On* and *Off* regions is equal to  $0.06\pi$ , respectively [68]. The expected number of counts in the energy bin of width  $\Delta E_k$  for each event type  $i$  is given by

$$\mu_{\text{limb},ik} = N_{\text{limb}} \int_{\Delta E_k} dE (E/E_0)^{-\Gamma_1} \left( 1 + (E/E_b)^{(\Gamma_1 - \Gamma_2)/\beta} \right)^{-\beta} \mathcal{E}^i(E), \quad (9)$$

where  $\mathcal{E}^i(E)$  is the exposure averaged over the full sky. The limb spectrum is modeled with a smooth broken power law to account for the effect of the Earth's geomagnetic cutoff. Following [76], we fix the parameters controlling

<sup>6</sup> [http://fermi.gsfc.nasa.gov/ssc/data/analysis/LAT\\_caveats.html](http://fermi.gsfc.nasa.gov/ssc/data/analysis/LAT_caveats.html)

<sup>7</sup> For the actual data analysis of the Vela pulsar and the Limb we use slightly broader energy windows.

<sup>8</sup> [http://www.slac.stanford.edu/~kerrm/fermi\\_pulsar\\_timing/](http://www.slac.stanford.edu/~kerrm/fermi_pulsar_timing/)

<sup>9</sup> <http://www.atnf.csiro.au/research/pulsar/tempo2/>

<sup>10</sup> The spectral model for a power law spectrum with super-exponential cutoff is defined though  $dN/dE = N(E/E_0)^{-\gamma_1} \exp((E/E_c)^{\gamma_2})$ .

the spectrum below and around the cutoff, namely  $E_b = 370.3 \text{ GeV}$ ,  $\Gamma_1 = 1.5232$ , and  $\beta = 0.7276$ , whereas the normalization  $N_{\text{limb}}$  and the spectral index above the cutoff  $\Gamma_2$  are free parameters. The reference energy is fixed to the central energy of the energy bin where the number of excess counts ( $n_{\text{excess}} = n_{\text{On}} - n_{\text{Off}}$ ) divided by its uncertainty is maximal. The expected number of counts of the background is calculated in the same way, assuming however a simple power law as the spectral model. We neglect the energy dispersion since both spectra for the limb and the background are smooth functions in energy that do not exhibit a cutoff in the considered energy range. The fit residuals above 5 GeV are shown in Fig. 7.

We use the residuals to estimate the maximum possible effect of small-scale structures in the exposure in the following way. We define a correction function  $c_i(E)$  for each event type  $i$  that is equal to  $P_{\gamma\gamma}$  if the amplitude of  $P_{\gamma\gamma}(E)$  is smaller than the absolute value of the fractional residual at energy  $E$ . Otherwise,  $c_i(E)$  is equal to the maximum amplitude of the absolute value of the fractional residual at energy  $E$ . We then divide each exposure by the corresponding  $c_i(E)$ . In this way, irregularities with an amplitude smaller than the fractional residuals will be removed and irregularities with larger amplitudes will be reduced. The maximum amplitude of the  $c_i$  functions is given by the maximum of the absolute value of the residuals in Fig. 7. However, we find that the limits are practically unchanged. The reason is that ALP parameters that are excluded at 95% confidence lead to irregularities of a larger amplitude than what can be counter-acted by possible small scale structures in the exposure.

	Vela pulsar	Earth limb
Time range (MET)	239846401–403747203	239557417–428859819
Energy range	100 MeV–10 GeV	1 GeV–100 GeV
LAT rocking angle	–	> 52°
ROI size	10° × 10°	Full sky

TABLE III. Basic data selection cuts for the analysis of the Vela pulsar and the Earth limb.

*Broadening of the energy dispersion.* We investigate the effect on the ALP limits in the case that energy resolution is worse than anticipated. The energy dispersion matrix of each event type is broadened along the reconstructed energy axis by the transformation  $\mathcal{D}_{kk'}^i(E, E') \rightarrow (1 - \epsilon)\mathcal{D}_{kk'}^i(E, E' - \epsilon(E' - E))$ . The ALP analysis is repeated with the degraded energy dispersion for  $\epsilon = 5\%$ ,  $10\%$ , and  $20\%$ . The results are shown in Fig. 8 (left panel). The fraction of excluded ALP parameters on the tested grid decreases by 6%, 11%, and 25%, respectively, for the choices of  $\epsilon$  above. The effect of the degraded energy dispersion is most visible around the “hole”-like feature where fast oscillating irregularities are present over the entire energy range accessible to the LAT. These irregularities are more likely to be flattened out by the degraded energy dispersion.

#### *Intra-cluster magnetic field*

The magnetic field of the Perseus cluster on scales of tens and hundreds of kpc is unknown due to the lack of Faraday rotation measurements [33]. We therefore investigate how the limits change if we alter the fiducial assumptions for the  $B$ -field calculation.

For fixed ALP parameters of  $g_{11} = 1$  and  $m_{a,\text{neV}} = 3$ , Fig. 9 shows the difference in the likelihood  $\Delta \ln \mathcal{L}$  that is obtained for different magnetic-field parameters. Higher values of  $\Delta \ln \mathcal{L}$  correspond to stronger exclusions. In each panel, all other  $B$ -field parameters are fixed to their fiducial values. We choose again the random  $B$ -field realization that results in the  $Q_B = 0.95$  quantile. The top right panel shows the dependence on the central magnetic field. Increasing the  $B$  field from  $2 \mu\text{G}$  to  $7 \mu\text{G}$  leads to a sharp increase in  $\Delta \ln \mathcal{L}$ . Above  $7 \mu\text{G}$ , the photon-ALP mixing is maximal and changing the  $B$ -field changes the shape of the irregularities (but not their amplitude) leading to the fluctuations of  $\Delta \ln \mathcal{L}$ . In the top central panel, the dependence of the radial magnetic field on the electron distribution is increased, where higher values of  $\eta$  correspond to a stronger decrease of the  $B$  field with radius. Surprisingly, the likelihood difference increases above  $\eta = 0.5$ . Inspecting the photon survival probability  $P_{\gamma\gamma}$  one sees that the very rapid oscillations become suppressed for higher values of  $\eta$  whereas larger features are more pronounced leading to stronger exclusions. The situation is similar when one increases the distance from the cluster center up to where we assume a non-zero  $B$  field (top left panel of Fig. 9). Naively one would assume that the considered ALP parameters should be more constrained for larger cluster radii. However, while the overall amplitude of the oscillation does not change, the frequency decreases with smaller radii leading to potentially broader irregularities that are not washed out by the energy dispersion.

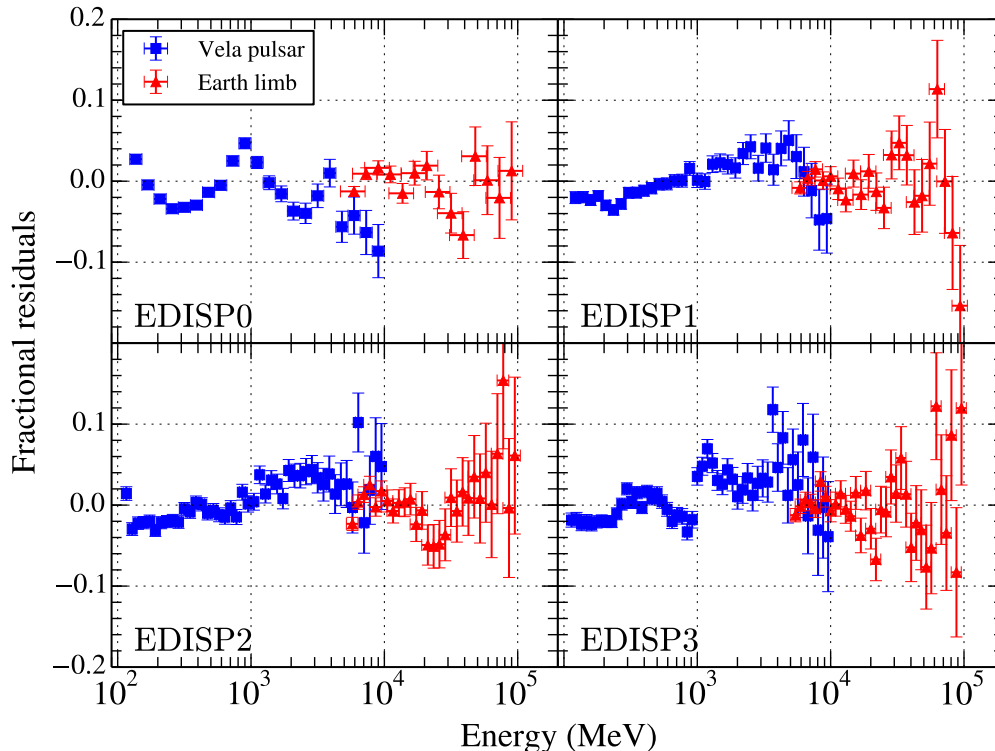


FIG. 7. Fractional residuals of the fits to the Vela pulsar and Earth limb used to estimate the amplitude of spectral features induced by energy-dependent biases in the effective area. The residuals are defined as the differences between the observed and expected counts divided by the expected counts.

The lower row of Fig. 9 shows the dependence on the parameters of the turbulence spectrum. Changing these parameters will also change the coherence length of the transversal magnetic field  $B_{\perp}$  [40],

$$\Lambda_c = \frac{1}{\langle B_{\perp}(\mathbf{x})B_{\perp}(\mathbf{x}) \rangle} \int_0^{\infty} dx_3 \langle B_{\perp}(\mathbf{x})B_{\perp}(\mathbf{x} + x_3\hat{\mathbf{e}}_3) \rangle, \quad (10)$$

where  $x_3$  is the axis along the line of sight. The fiducial parameter set results in a coherence length of  $\Lambda_c \sim 1.32$  kpc. For softer turbulence spectra, i.e. smaller values of  $q$ , the coherence length increases as large spatial scales become more dominant. This leads to broader irregularities in energy, and, subsequently, to larger ALP exclusion areas. For  $q \rightarrow 0$ , the turbulence spectrum resembles white noise resulting in fast oscillations of  $P_{\gamma\gamma}$  with energy.

The situation is less obvious when changing the minimum wave number,  $k_L$  (or maximum turbulence scale). Even though  $\Lambda_c$  slightly decreases with increasing  $k_L$ , strong maxima are visible in the likelihood difference (bottom central panel of Fig. 9). These correspond to cases where  $P_{\gamma\gamma}$  exhibits strong isolated peaks at the onset of the irregularities that are in strong tension with the data. These peaks are also seen in Fig. 4 between 100 MeV and 1 GeV, however not as isolated. Our fiducial parameter choices do not lead to such features and can be regarded as conservative in this respect.

Increasing the maximum wavenumber  $k_H$  above its fiducial value has only a very small effect on the likelihood and the coherence length. With increasing  $k_H$ , the frequency of the oscillations around the critical energy is also increased, yet, when folded with the energy dispersion, these features are not detectable anymore.

In conclusion, the derived ALP limits depend sensitively on the assumed  $B$ -field parameters. We quantify the effect further by repeating the limit calculation for all ALP parameters but changing one  $B$ -field parameter at a time. The excluded regions are shown in Fig. 8 (right). We limit ourselves to  $\sigma_B$ ,  $q$ , and  $r_{\max}$ . Increasing  $\sigma_B$  to  $20 \mu\text{G}$  allows us to exclude smaller values of the photon-ALP coupling thanks to the full degeneracy of  $B$  and  $g_{a\gamma}$ . The higher



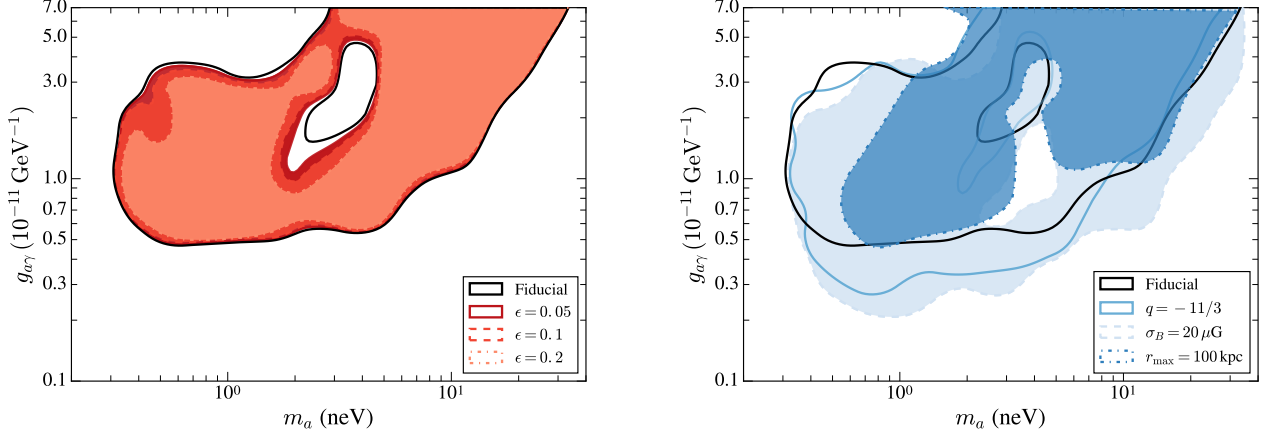


FIG. 8. *Left*: Upper limits re-calculated for a degraded energy dispersion. *Right*: Upper limits re-calculated with different assumptions on the central magnetic-field strength ( $\sigma_B = 20 \mu\text{G}$ ), the turbulence spectrum ( $q = -11/3$ ), and the spatial extent of the magnetic field in the cluster ( $r_{\text{max}} = 100 \text{ kpc}$ ).

value of  $\sigma_B$  is close to the measurement reported in [33] of  $25 \mu\text{G}$ . As a result, the excluded region of ALP parameters increases by 43%. Similarly, assuming a Kolmogorov-type turbulence spectrum,  $q = -11/3$ , as observed e.g. in Hydra A [51] and Coma [77], increases the excluded parameter region by 12%. In this case, the coherence length increases to  $\Lambda_c = 2.89 \text{ kpc}$ . Decreasing the maximal distance up to which the magnetic field is non-zero to 100 kpc leads to a decrease by 16%, even though it might increase the significance of the exclusion for some ALP parameters as noted above.

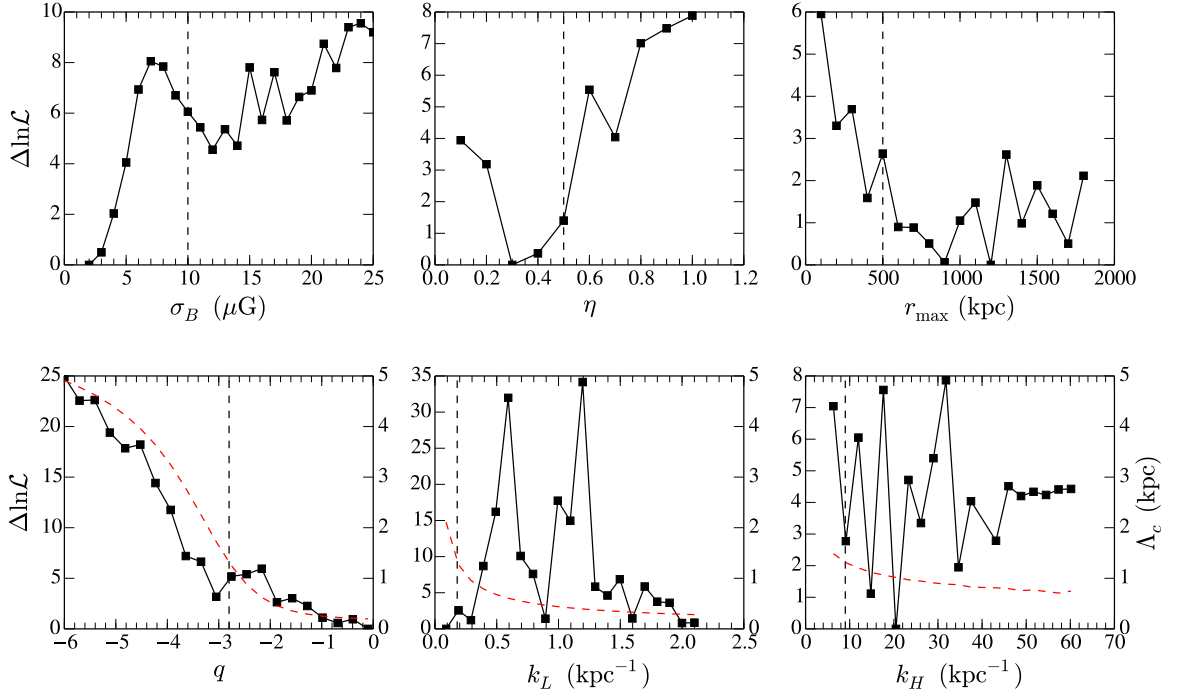


FIG. 9. Dependence of the maximum likelihood on the  $B$ -field parameters for fixed ALP parameters,  $m_{a,\text{neV}} = 3$  and  $g_{11} = 1$ . From left to right and top to bottom the tested parameters are the variance of the magnetic field ( $\sigma_B$ ), the index of the radial dependence of the  $B$  field on the electron density ( $B(r) \propto n_e(r)^\eta$ ), the maximal spatial extent of the  $B$  field ( $r_{\text{max}}$ ), the index of the turbulence spectrum ( $q$ ), and the wave numbers corresponding to the maximum ( $k_L$ ) and minimum ( $k_H$ ) turbulence scales. For the lower panel, the transversal coherence length  $\Lambda_c$  of the magnetic field is also shown (red dashed line and right  $y$ -axis). The vertical dashed lines denote the fiducial parameters.